Functional graded NiTi manufactured with powder bed fusion

Progress in Additive Manufacturing
https://doi.org/10.1007/s40964-024-00584-2

FULL RESEARCH ARTICLE

Functional graded NiTi manufactured with powder bed fusion

Rico Weber[1,2] · **Enrico Tosoratti**[1] · **Adriaan B. Spierings**[1] · **Konrad Wegener**[2]

Received: 24 October 2023 / Accepted: 4 February 2024

Abstract
Nickel–titanium (NiTi) is a versatile material with unique inherent properties, such as shape recovery, superelasticity, and biocompatibility, that makes it suitable for various engineering applications. While NiTi can be additively manufactured using powder bed fusion for metals (PBF-LB/M), challenges arise due to the material sensitivity to process parameters and the challenge of achieving desired mechanical and functional properties. Mechanical and functional properties of NiTi are highly influenced by the alloy composition which in turn is affected by the process parameters. This study aims to investigate the feasibility of tailoring the properties of NiTi to manufacture functionally graded structures. Promising shape recovery strains of 4.16% and superelastic strains of 7% under compression are achieved with cycling stability outperforming the conventional manufactured NiTi. By varying the process parameters, the austenite finish temperature could be shifted between 29 ± 5 °C and 72 ± 5 °C, while achieving a maximum relative material density of 99.4%. Finally, the study demonstrates the potential of powder bed fusion to manufacture complex and functional graded structures, enabling spatial control. This potential is showcased through the sequential actuation of a demonstrator structure. The findings of this research highlight the promising capabilities of powder bed fusion in producing functional graded NiTi structures, with potential applications in robotics, aerospace, and biomedical fields.

Keywords Additive manufacturing · Shape memory · 4D printing · NiTi

1 Introduction

NiTi has gained significant interest due to its unique characteristics, such as shape memory, superelasticity, and biocompatibility. The underlying diffusionless and reversible phase transformations between martensite B19' and austenite B2 phase govern the phase transformation behavior [1]. In recent years, the potential applications of NiTi have been enhanced by the ability to produce complex parts using powder bed fusion [2]. Additive manufacturing offers distinct advantages, particularly for NiTi parts, as it enables the production of near-end shape geometries, which are challenging to achieve through machining [3–5]. While commercially available NiTi parts mostly consist of standard geometries, such as springs and wires [6], powder bed fusion presents significant potential for expanding the range of applications by facilitating the realization of complex and near-end shape geometries. NiTi alloys are increasingly playing an important role in aerospace applications, surgical instruments, and medical fields [7]. For instance, the shape memory effect of NiTi provides an excellent opportunity to replace heavy electrical, pneumatic, or hydraulic actuators in aerospace [8].

It is widely recognized that the transformation behavior of NiTi is primarily governed by the Ni content with a change in transformation temperature of 100 K per 1% change of Ni at% [9]. A higher Ni content leads to lower transformation temperatures in terms of As, Af, Ms, Mf (austenite and martensite start and finish temperatures), as well as Ap and Mp (austenite and martensite peak temperatures). Processing with powder bed fusion leads to complex thermal histories and solidification rates due to the melting and reheating of consecutive layers. As a result, significant effects on the chemical composition as well as on precipitates, residual stress, and microstructure can be observed influencing the phase transformation behavior and, therefore, functional

✉ Rico Weber
riweber@ethz.ch

[1] Inspire AG, Innovation Center for Additive Manufacturing Switzerland (ICAMS), Lerchenfeldstrasse 3, 9014 St. Gallen, Switzerland

[2] Swiss Federal Institute of Technology, ETH Zürich, Institute of Machine Tools and Manufacturing (IWF), Leonhardstrasse 21, 8092 Zürich, Switzerland

Published online: 15 April 2024

and mechanical properties [10–12]. Dadbakhsh et al. [13, 14] have reported a maximum relative densities of >99% when manufacturing NiTi using powder bed fusion. Several studies were conducted to investigate the influence of process parameters and energy density on transformation temperatures of NiTi [10, 14–17]. Higher energy densities resulted in a decrease of Ni content due to Ni evaporation and shifted transformation temperatures to higher values [10, 18]. However, higher energy densities also increased impurity pick-up of oxygen and carbon resulting in Ti-rich phases ($Ti_4Ni_2O_x$, TiO_2, TiC). This causes titanium depletion and increasing Ni content in the matrix, whereas Ni evaporation remains the principal factor in the shift of transformation temperatures [16].

Several functional properties of NiTi such as shape memory and superelasticity fabricated using powder bed fusion have been investigated in the literature. Compression tests reported shape recovery strains ranging between 3.95 and 5.5% after heating, with cycling degradation after 10–15 cycles [16, 19]. In comparison, the conventional NiTi can achieve up to 8% strain recovery after heating [20]. The variation in laser power, scanning speed, or hatch distance did not show a significant effect on shape recovery rate [10]. However, different processing parameters were observed to affect the plateau stress at which stress-induced martensite reorientation occurs. Higher plateau stresses can be achieved by increasing the scanning speed or hatch spacing, or by decreasing laser power while keeping the other parameters constant [10]. Besides shape memory properties, superelasticity enables high strains without plastic deformation. Superelastic strains between 4 and 5.6% were reported with high cycling stability and minimal degradation [16, 21]. In comparison, conventional NiTi has achieved superelastic strains of 6–7% [22].

In this study, the processing of NiTi using Ni-rich powder on an industrial powder bed fusion machine was conducted, with a focus on the potential and limitations of tuning the transformation temperature, which is crucial for applications. The unique ability to set different transformation temperatures and switch between shape memory and superelasticity properties in powder bed fusion produced NiTi samples allows for the manufacturing of monolithic graded structures which is not feasible with the conventional NiTi processing. By controlling the transformation temperatures, NiTi parts with different thermal activation sequences and spatial control can be used, e.g., in gripper systems or actuators. Dense NiTi parts were manufactured with a wide range of energy densities (74–222 J/mm^3). DSC (differential scanning calorimetry) analysis of as-built and heat-treated samples provided insights into the transformation behavior and tunability. It is important to consider the variability and uncertainties of transformation behavior, which are often overlooked in literature but play a crucial role in the tuning process. This study also provided insight into the measurement accuracy of transformation temperatures.

While many researchers performed compression tests below or above Af [10, 16, 21], this study conducted tests at a fixed room temperature (19 °C) to investigate the capability to manufacture mechanical graded structures. Moreover, this study investigated the variation in the transformation behavior for samples with the same energy densities but different laser power and scanning speed combinations to contribute to similar studies [10, 19]. Additionally, the effect and influence of feature size, such as changes in the wall thickness, on transformation behavior were investigated. Finally, a complex structure with thermal grading was successfully actuated, demonstrating the capabilities of powder bed fusion manufactured NiTi parts.

2 Materials and methods

2.1 Machine, powder, and process parameters

NiTi powder was processed in an argon atmosphere on a Concept Laser M2 machine (Concept Laser GmbH), which is equipped with a Nd-YAG fiber laser with a maximum continuous power of 400 W at a wavelength of 1064 nm. Chamber oxygen content during processing was relatively high with ~ 0.45 %. The NiTi powder was pre-alloyed and supplied from TLS Technik (Germany) with 55.2 ± 0.7 wt% Ni measured with Energy Dispersive X-Ray Analysis (EDX) (Zeiss Evo 10 equipped with Oxford instruments EDX). The particle-size distribution is illustrated in Fig. 1b measured with a median particle size (d_{50}) of 42.1 μm (Bettersizer S3 Plus). Furthermore, Fig. 1c presents the DSC curve of the powder, revealing an Af of 35 °C. The DSC analysis also indicates a multi-step transformation with two peaks during heating and three peaks during cooling. For comparison, a conventionally manufactured 3 mm in diameter NiTi wire was acquired from Nexmetal with 55 wt% Ni and austenite finish of 60 °C, as specified by the supplier.

The process parameters listed in Table 1 were selected to cover a wide range of energy densities, ranging from the lowest value of 74 J/mm^3 to the highest value of 222 J/mm^3. Previous research was conducted with energy densities ranging from 28 to 412 J/mm^3, with the range of 40–170 J/mm^3 considered as low–medium-energy densities and above 170 J/mm^3 considered as high-energy densities [17]. It is worth noting that high-energy densities, which are also investigated in this study, are underrepresented in the literature [17]. In this study, scan speed was varied within the range of 150–300 mm/s and laser power from 80 to 120 W. The hatch distance, spot size, and layer thickness were kept constant throughout the experiments.

Table 1 Process parameters, relative density, and energy density of all samples manufactured

Sample	Power (W)	Speed (mm/s)	Hatch (mm)	Layer thickness (mm)	Spot size (mm)	Rel. density[a] (%)	Energy density[b] (J/mm^3)
1	80	150	0.12	0.03	0.08	99.0	148
2	80	200	0.12	0.03	0.08	99.2	111
3	80	250	0.12	0.03	0.08	99.4	89
4	80	300	0.12	0.03	0.08	99.4	74
5	100	150	0.12	0.03	0.08	98.5	185
6	100	200	0.12	0.03	0.08	98.8	139
7	100	250	0.12	0.03	0.08	99.0	111
8	100	300	0.12	0.03	0.08	99.2	93
9	120	150	0.12	0.03	0.08	96.1	222
10	120	200	0.12	0.03	0.08	97.7	167
11	120	250	0.12	0.03	0.08	98.5	133
12	120	300	0.12	0.03	0.08	99.0	111

[a]Mean value measured with archimedes method using a raw density of 6.45 g/cm^3

[b]Energy density is calculated as following $E = P/(v \times h \times t)$ with P *laser powder*, v *scanning speed*, h *hatch distance*, and t *layer thickness*

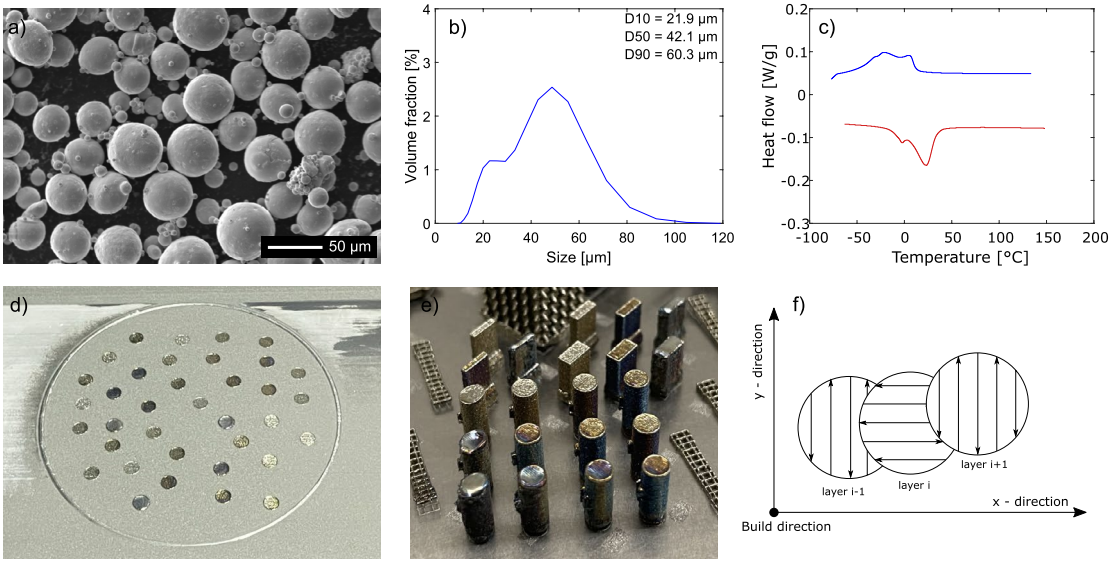

Fig. 1 **a** SEM image of NiTi powder; **b** particle-size distribution of powder; **c** DSC measurement of powder with multiple peak transformation; **d** 5 mm cylindrical samples on the build plate for DSC analysis; **e** 3 mm cylindrical samples for compression tests and samples of different wall thickness for investigation of geometrical influence; **f** scan strategy with 90° scan vector rotation in each consecutive layer

2.2 Sample preparation

Cylindrical samples of 6.4 mm length with 5 mm diameter were manufactured with the process parameters listed in Table 1 to investigate the transformation temperatures. Three samples (No. 2, No. 7, and No. 12) with the same energy density of 111 J/mm^3 but with different parameter combinations were manufactured. For each process parameter, three samples were built in three different positions on the build plate to investigate the variability (see Fig. 1d). For compression tests, cylindrical samples with 7.5 mm length and 3 mm diameter were made for each process parameter. The geometrical dependency of the transformation temperature was also explored. Therefore, structures with different wall thicknesses were built with low-, medium-, and high-energy densities. The geometrical influence was investigated for the wall thickness 0.8, 1.4, and 2 mm each build with 74, 148 and 222 J/mm^3 energy density, respectively. For all samples, the scanning strategy is displayed in Fig. 1f with a 90° rotation of hatch for each consecutive layer.

2.3 Measurement procedures

Density was determined using the Archimedes principle on three samples built in different positions for each process parameter. After grinding and polishing, cross-section imaging was performed using a Leica microscope (DM6). The transformation temperatures were determined using differential scanning calorimetry (DSC 25, TA instruments). To eliminate oxidation layers, grinding was performed on the 5 mm sample cylinders. DSC samples weighing 20–80 mg were extracted from the middle of the samples by cutting and grinding. The same preparation procedure was applied to samples with different wall thicknesses. The samples were heated to 150 °C above the Af temperature and maintained for 5 min to avoid partial transformation during the measurement. Subsequently, the samples were cooled to −80°C and then heated to 150 °C and finally cooled back to −80°C with a temperature ramp of 10 °C/min. At −80 and 150 °C, 1 min isothermal hold was implemented to ensure equilibrium. The transformation temperatures were determined using the tangent method. The phase proportions were determined by integrating the DSC curve over temperature. The area under the DSC curve is defined as the transformation heat. This transformation heat is proportional to the volume fraction involved in the phase transformation [23, 24]. Solution annealing was performed at 950 °C for 5.5 h with subsequent quenching with high-pressure argon gas flow at a rate of 1.7 °C/s.

Investigation of functional properties was done with compression tests on a Galdabini Quasar 10 (Galdabini). Surfaces of the 3 mm cylindrical samples were cut and ground to a planar shape before testing. Loading of the samples was done with 100 N/s to a maximum force of 3500 N which corresponds to 500 N/mm^2 to achieve detwinning of martensite, which occurs at 400 N/mm^2 [25, 26]. Subsequently, the load was reduced to 0 N at a rate of 100 N/s. After unloading, the samples were heated in boiling water to initiate the reverse transformation and shape recovery. This procedure was repeated 15 times to investigate the stability and degradation of the shape memory effect. The temperature during mechanical testing was held constant at room temperature of 19 °C to investigate the influence of partial transformation. The length of the samples was measured using a micrometer gauge before loading, after loading, and after heating. Displacements at 0 N and 3500 N were recorded using the tensile testing machine. Reverse transformation strain was calculated as the difference in length before and after heating, expressed as a percentage from the initial length before each compression cycle. The superelastic strain was calculated using the tensile test machine displacement during unloading from 3500 N to 0 N, also expressed as a percentage of the initial length. Hardness tests (LVD-302, ESI Prüftechnik) were performed on the as-built 3 mm cylindrical samples before and after compression as well as after solution annealing on the DSC samples. Before testing, surfaces were ground and polished to achieve equal surface roughness. The Vickers hardness HV1 was calculated by measuring the indentation with a microscope Leica microscope (DM6). Five measurement points were acquired to obtain a statistically representative measurement.

3 Results and discussion

3.1 Relative density and cross-section

The relative densities of the cylinders built with different process parameter combinations are shown in Fig. 2. Dense NiTi material is achieved with a maximum relative density of 99.4% when using a laser power of 80 W and a scanning speed of 250 mm/s. When using a laser power of 80 W, a relative density of ≥ 99% is achieved over a range of scanning speeds (150–300 mm/s), providing the potential to vary the energy density from 74 to 148 J/mm^3 without significantly compromising porosity. Similarly, the highest densities for laser powers of 120 W and 100 W are 99 and 99.2%, respectively. Lower scan speeds result in a decrease in density due to keyhole porosity. For all laser powers, dense material can be produced, which is crucial for tuning of material properties. Furthermore, samples produced with the same energy density of 111 J/mm^3 using different parameter combinations (80 W and 200 mm/s, 100 W and 250 mm/s, and 120 W and 300 mm/s) show similar relative densities, providing another option to tune the properties of NiTi without compromising material density.

The cross sections of NiTi samples processed with different parameters are shown in Fig. 3. The sample numbering

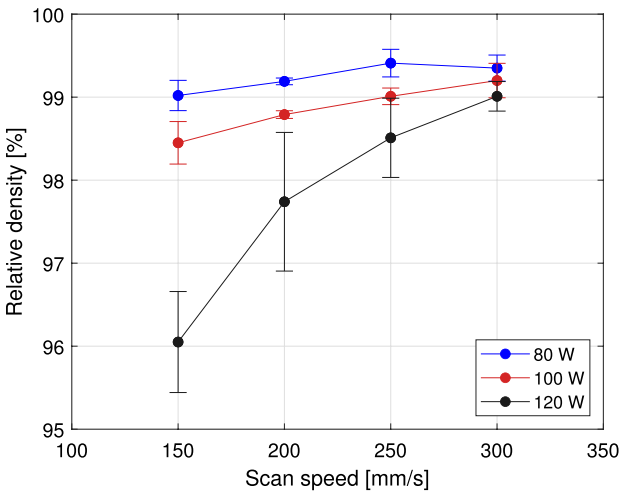

Fig. 2 Relative density plotted against scan speed for different laser power

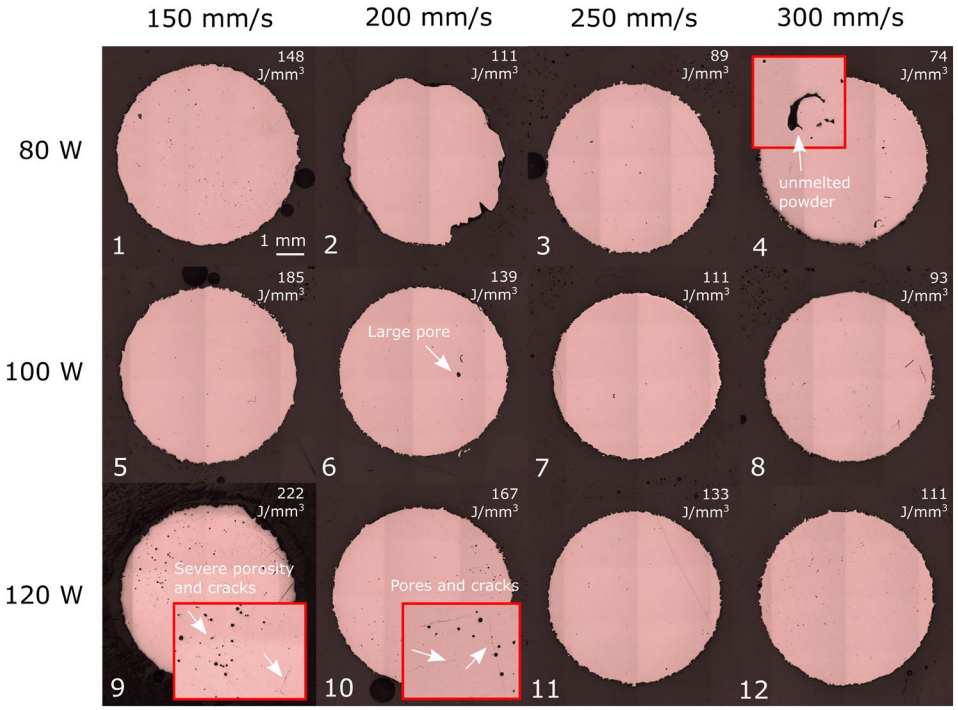

Fig. 3 Cross section of the samples manufactured according to Table 1 with scanning speeds 150, 200, 250, and 300 mm/s for samples 1–4, respectively (fixed power 80 W and hatch 0.12 mm). For samples 5–6, power was set to 100 W, and for samples 9–12 to 120 W, with scanning speeds 150, 200, 250, and 300 mm/s and hatch 0.12 mm fixed

corresponds to Table 1. The measured relative density obtained using Archimedes method is well represented in the optical cross-sectional images. Sample 9 with the lowest relative density of 96.1% is manufactured with an energy density of 222 J/mm^3. This sample shows significant porosity and cracks. In sample 4, the presence of unmolten powder is observed, which can be attributed to the low-energy density of 74 J/mm^3, resulting in a lack of bonding. In the cross sections, sample 12 contains more pores compared to sample 7 despite both samples being manufactured with the same energy density.

3.2 Transformation behavior

With DSC measurements, the transformation behavior is investigated. The DSC charts for all as-built samples are presented in Fig. 4a. First, it is observed that the transformation behavior from the powder with its multiple peaks changes into a single-step B19' to B2 transformation for low and medium energy densities, exhibiting multiple peak transformation again for higher energy densities. The DSC curve for the lowest energy density has a similar Af temperature compared to the powder. Overall, transformation temperatures increase with increasing energy density. Peaks associated with low-energy densities appear flat and broad, covering a wide range of temperatures during transformation, while medium energy densities show sharp and narrow peaks. Inhomogeneities due to secondary phases are attributed as causes for broad peaks and were also observed by other researchers [10, 16]. This observation is also supported by the cross-section of sample number 4 in Fig. 3, which was manufactured with the lowest energy density and showed unmolten powder.

The double-peak transformation during heating for higher energy densities in Fig. 4a is attributed to the formation of R-phase. The R-phase is energetically preferred over B19' in the presence of Ni4Ti3 precipitates [22, 27, 28]. Due to the high oxygen content during processing other factors which make the R-phase more preferable, e.g., impurities could also lead to the preference of the R-phase and formation of the double peaks in the DSC. This is supported by similar DCS curves from Haberland et al. [16], who also processed Ni-rich powder in a high oxygen atmosphere with high energy densities. It is well known that the transformation temperature of NiTi is dependent on the Ni content, where a decrease in Ni content leads to higher transformation temperatures [9]. With higher energy input into the melt pool through higher laser power, slower scan speed, or smaller hatch distance, the melt pool temperatures increase and reach the boiling point of Ni and Ti. Due to the lower vapor pressure of Ni compared to Ti, more Ni evaporates compared to Ti, resulting in Ni depletion and a shift of the transformation temperatures to higher values [10, 18].

Figure 5 presents the transformation temperatures for both the as-built and solution annealed conditions, whereby As, Ap, and Af are austenite start, peak, and finish temperatures and Ms, Mp, and Mf martensite start, peak, and finish temperatures, respectively. The Af temperature, which defines the end temperature for shape recovery, is particularly interesting for actuating applications. In this study, the

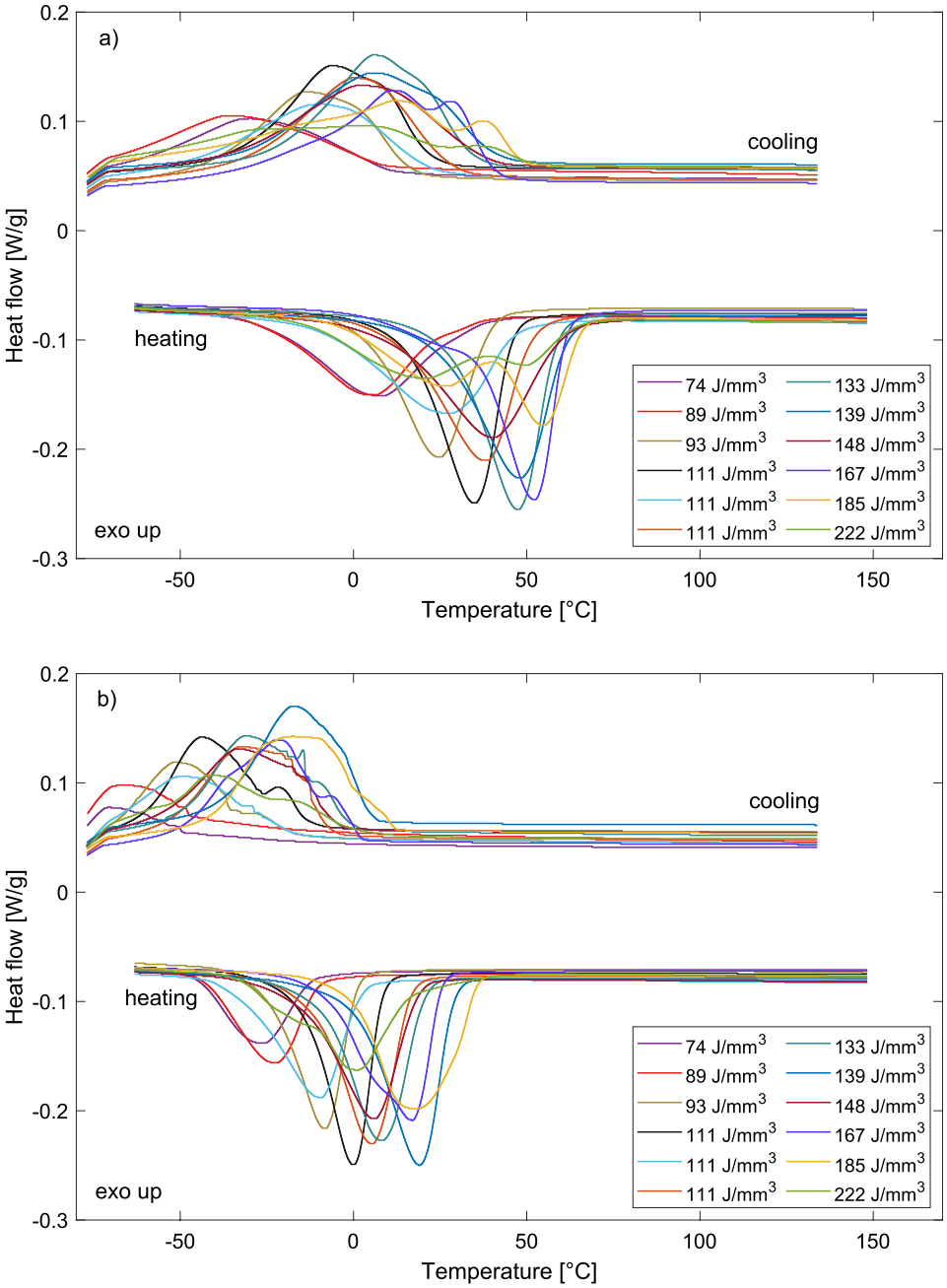

Fig. 4 DSC measurements of **a** as-built and **b** solution annealed samples (950 °C for 5.5 h) for low (74–93 J/mm^3), medium (111–167 J/mm^3), and high (185–222.2 J/mm^3) energy density

Af temperature can be tuned between 29 ± 5 °C and 72 ± 5 °C for the as-built condition, offering the potential for the development of graded NiTi structures. For the highest energy density of 222.2 J/mm^3, the standard deviation in some cases is exceptionally high due to multiple and broad peaks, which increase the difficulty of determining precise transformation temperatures.

The decrease in transformation temperatures observed after solution annealing at 950 °C for 5.5 h, followed by quenching with pressurized argon at a cooling rate of 1.7 °C/s (see Fig. 4b), is attributed to several factors. Besides the sharpening of peaks due to the dissolution of inhomogeneities, the enthalpy of the R-phase peak in the heating curve for the energy density of 185 J/mm^3 is reduced but still present. This suggests that the slow cooling rate of 1.7 °C/s, in comparison to water quenching, was insufficiently slow to keep the precipitates completely dissolved. The decrease in transformation temperatures shown in Fig. 5 after solution annealing indicates the formation of precipitates that influence the Ni/Ti ratio or impede the transformation process. The Ap temperature of the solution annealed samples is consistently 33 °C lower on average compared to as-built samples, which seems to remain constant across the range of energy densities. Similar findings were reported by

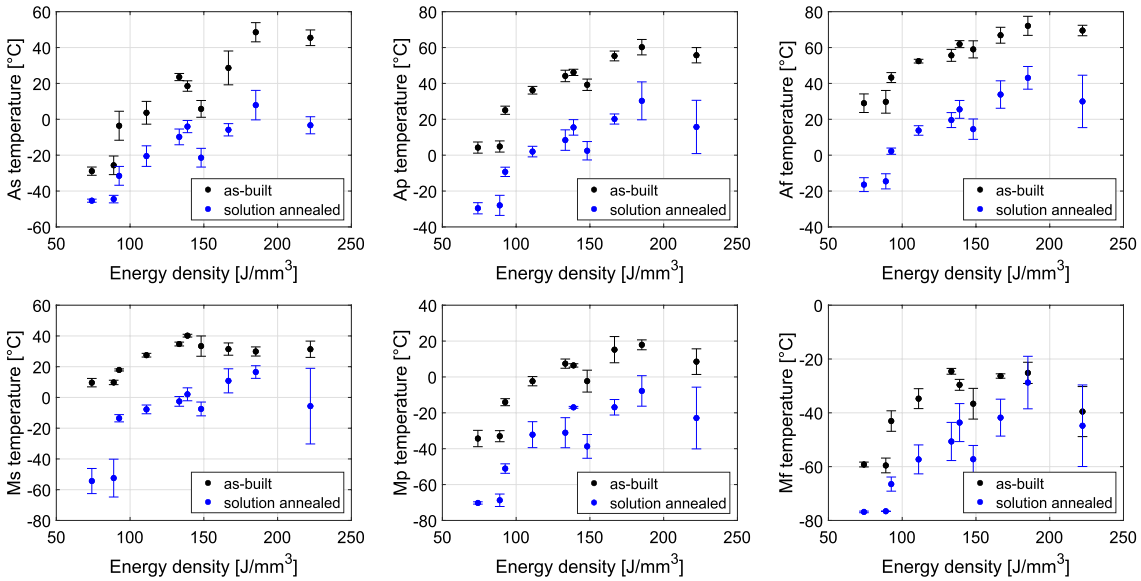

Fig. 5 Transformation temperatures with mean value and standard deviation plotted against energy density whereby As, Ap, and Af are austenite start, peak, and finish temperatures and Ms, Mp, and Mf martensite start, peak, and finish temperatures, respectively, for as-built and solution annealed conditions. Only data of sample 7 are plotted from the same energy density samples of 111 J/mm^3

Bormann et al. [29], who observed a 20 °C decrease of austenite peak temperatures after solution annealing at 800 °C for 30 min in argon atmosphere, followed by water quenching. In their study, XRD measurements revealed $Ti_4Ni_2O_x$ precipitates after solution annealing, which lead to Ti depletion and therefore to an increase of Ni in the matrix and decrease of transformation temperatures [29]. In literature, solution annealing is often performed using water quenching, and a consistent decrease in peak transformation temperatures of only 5–10 °C for solution annealed samples is observed compared to as-built samples [10, 15, 30]. The presence of high oxygen content in the build chamber during processing, present also in the study of Bormann et al. [29], could lead to more pronounced impurity pick-up, formation of Ti-rich precipitates during heat treatment, and consequently different shifts of the transformation temperature across various studies.

3.3 Processing with same energy density

Due to the high sensitivity of the transformation behavior to the process parameters, three samples with the same energy density of 111 J/mm^3, but different laser power and scanning speed combinations were manufactured. The DSC curves are presented in Fig. 6 and show deviations in start, finish, and peak temperatures. Taking into account the standard deviation of the measurement shown in Fig. 5, the parameter set of 80 W and 200 mm/s exhibits lower transformation temperatures compared to the other samples manufactured with the same energy density of 111 J/mm^3, except for the Af temperature. Furthermore, there is a specific combination of process parameters leading to sharp and narrow peaks. The parameters with the lowest power and lowest scan speed lead to inhomogeneities and broad peaks. This provides evidence that the process parameters directly influence the thermal history of the melt pool, consequently affecting the chemical composition and microstructure, which significantly alter the transformation behavior at the same energy density levels. The

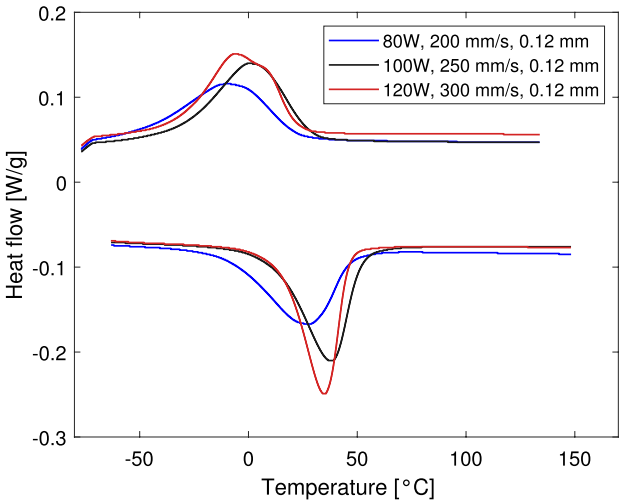

Fig. 6 DSC measurements for as-built samples manufactured with the same energy density of 111 J/mm^3 but different process parameter combinations of power and speed (hatch distance fixed)

deviation in transformation behavior for the same energy densities also seems to be more pronounced at higher energy densities [10, 19]. To conclude, the energy density is not a favorable parameter to tune the transformation temperature of NiTi. Instead, the precise combination of process parameters is crucial for obtaining reproducible results.

3.4 Geometrical influence on transformation behavior

The manufacture of complex NiTi structures leads to variations in their cross-sectional areas. For this reason, the variation of the cross-section area and its impact on the transformation behavior is investigated. Three different wall thicknesses of 0.8, 1.4, and 2 mm were built with low (74.04 J/mm^3), medium (148 J/mm^3), and high (222 J/mm^3) energy densities using the parameters specified in Table 1. Figure 7 presents the results obtained from the DSC analysis. The findings indicate that the wall thickness does not significantly influence the transformation temperatures. However, slight deviations in the transformation behavior could still be observed. Regardless of the energy density, the enthalpy (i.e., transformation heat) increases as the wall thickness decreases. There is a dependency between enthalpy and energy density in literature. The enthalpy is increasing for higher energy densities [10, 11]. Consequently, reducing the wall thickness has a similar effect on the enthalpy as an increase in energy density. The DSC curves for the higher energy density need to be considered separately due to their multi-step transformations. While the R-phase can be detected in the DSC for all wall thicknesses processed with high energy density, the double peak during heating gets most pronounced for the 0.8 mm wall thickness. Due to the dependency of energy density, enthalpy, and wall thickness, the wall thickness influences the cooling rate of the part and therefore also the in-situ aging effects resulting in different sized Ni4Ti3 precipitates [11]. Smaller wall thickness causes slower cooling rates, similar to higher energy densities, and therefore a more pronounced R-phase transformation due to precipitates. Guo et al. [15] also observed an increase in enthalpy for smaller wall thicknesses and the diminishing

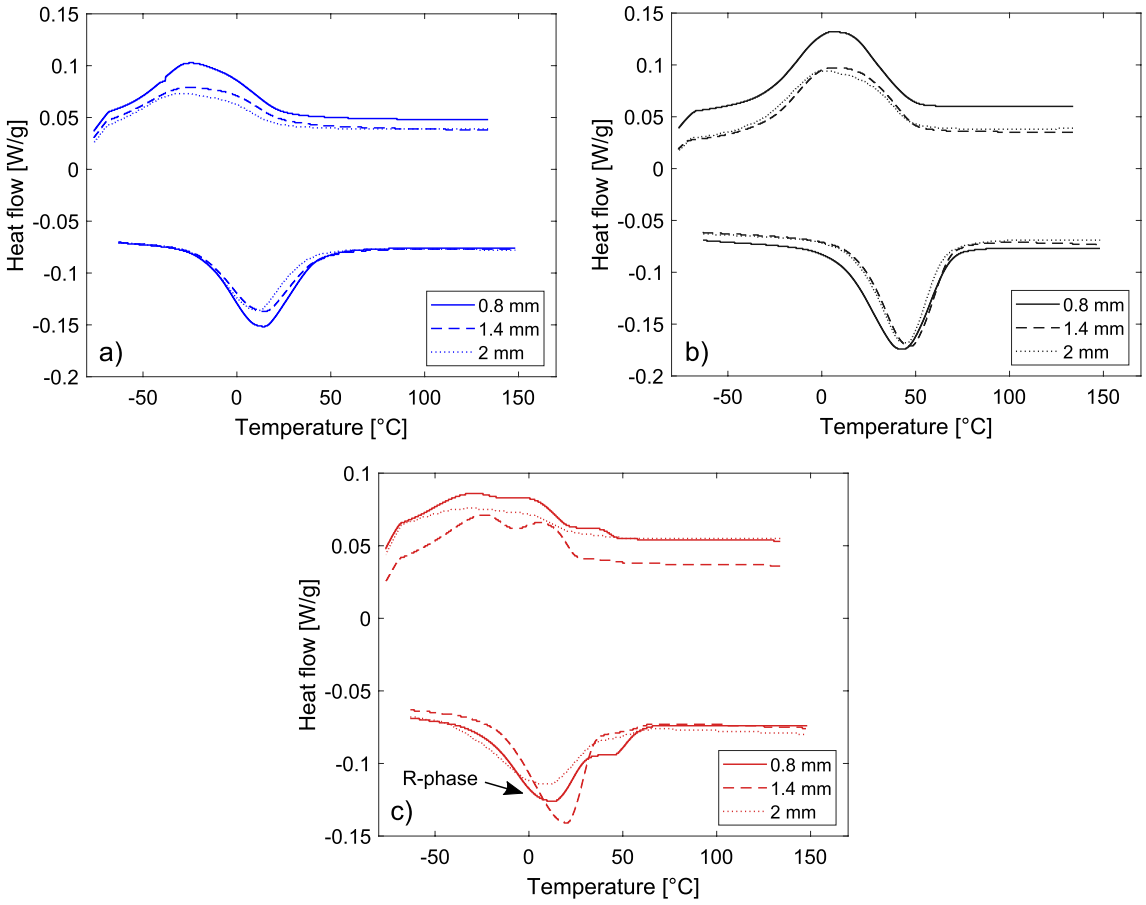

Fig. 7 DSC measurements of different wall thicknesses 0.8, 1.4, and 2 mm each manufactured with **a** low- (74.04 J/mm^3), **b** medium- (148 J/mm^3), and **c** high-energy density (222 J/mm^3)

influence of geometry at higher energy densities. However, Guo et al. [15] only reported an influence for energy densities of ≤ 60 J/mm^3. Consequently, when designing and manufacturing complex NiTi structures, the geometric influence on the transformation behavior is more significant for lower energy densities than for higher ones.

3.5 Compression tests

Compression tests were performed to investigate the shape memory and superelasticity performance of powder bed fusion manufactured NiTi parts in comparison to conventionally manufactured NiTi parts. Previous studies on compression testing have primarily focused on testing above Af to achieve full B2 austenite phase and superelastic properties [21, 31]. Instead, in this study, compression tests were performed at room temperature (19 °C) to investigate the influence of partial B19' and B2 phase and the capability to manufacture mechanical graded structures. Figure 8 presents cycling compression tests performed to investigate the stability of the reverse transformation strain ϵ_r and superelastic strain ϵ_{se} over 15 cycles. The stress–strain curves with the phase proportions at testing temperature are shown in Fig. 8 and exhibit typical

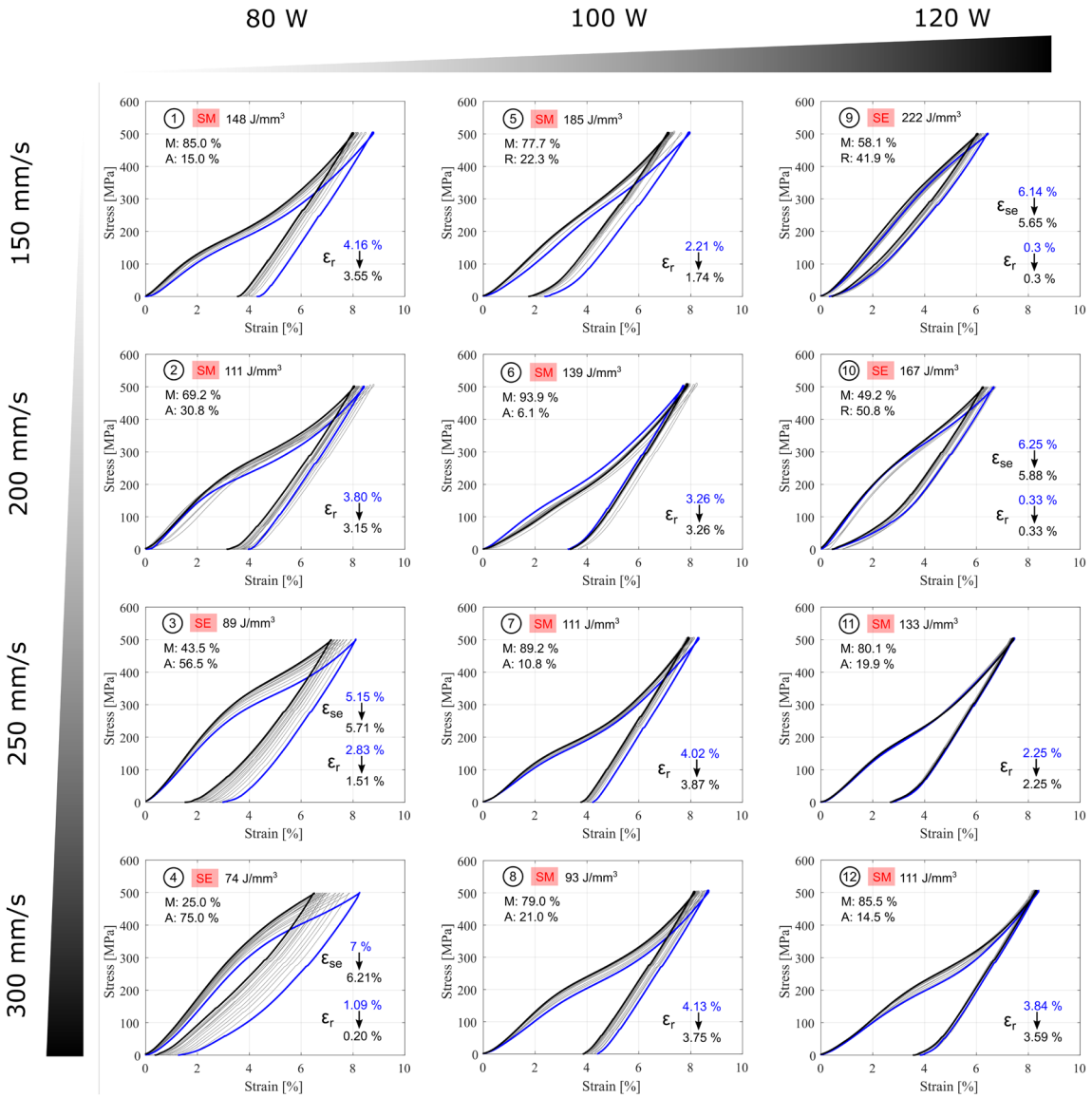

Fig. 8 Compression tests with 15 cycles performed at room temperature (19 °C) for all samples from Table 1. Shape memory behavior is marked with SM and superelasticity with SE. Martensite (M), austenite (A), and R-phase (R) phase proportions are indicated in percentage. For all samples, reverse transformation strain after heating (ϵ_r) and superelastic strain (ϵ_{se}) is measured for cycle one (blue) and cycle 15 (black)

compression behavior associated with shape memory and superelasticity [32]. Higher energy densities (≥ 90 J/mm^3) lead to shape memory properties due to the elevated transformation temperature while testing at room temperature. This observation is also supported by an increasing proportion of the martensite phase with higher energy densities indicated by the phase proportions in Fig. 8. Conversely, low energy densities result in superelastic behavior caused by lower transformation temperatures. The transformation behavior characterized by double peaks is an exception and requires a separate analysis, since it occurs within the R-phase transformation temperature range. Shape memory behavior is observed when the martensite phase dominates over the austenite phase, whereas superelasticity is associated with a dominant austenite phase. For sample 3, the austenite phase accounts for only a slightly higher proportion (56.6%) over the martensite phase (43.5%), exhibiting a mixture of both phase properties. The stress–strain curve shows a superelastic behavior, albeit with a noticeable reverse transformation strain during shape recovery, which is not observed in the fully superelastic behavior as seen in samples 9, 10, and 4. Therefore, a mixture of both shape memory and superelasticity can be obtained by tuning the process parameters.

Analyzing the stress–strain curves of samples 5, 9, and 10 reveals the influence of the R-phase. It appears that when the R-phase becomes dominant beyond a certain threshold, the mechanical properties transition from shape memory to superelastic behavior. This can be seen by comparing the curve shape and sharp decrease of the reverse transformation strain from sample 5 to samples 9 and 10 in Fig. 8. Sample 5 exhibits shape memory behavior with a dominant martensite phase of 77.7%, while it switches to fully superelastic behavior for slightly dominant R-phase in sample 10, or even with R-phase proportions slightly below 50%. Remarkably, achieving full superelastic properties does not necessarily require an R-phase proportion of ≥ 50%. This behavior significantly differs from the case where martensite and austenite proportions are similar.

Cycling stability is an important criterion for evaluating the degradation of functional properties. In this study, the reverse transformation strain is measured after compression cycle 1 and 15. In addition, the superelastic strain was also assessed. Sample 1 achieved a maximum reverse transformation strain of 4.16% with an energy density of 148 J/mm^3, while sample 4 exhibited a maximum superelastic strain of 7% with an energy density of 74 J/mm^3. Comparable values for reverse transformation and superelastic strains in the literature are 3.95–5.5% [16, 19] and 4–5.6% [16, 21], respectively. Despite the high oxygen content during processing in this study, maximum strains do not appear to be significantly affected. The degradation of the reverse transformation strain after 15 cycles seems to be significantly lower for higher energy densities, although exceptions can be seen within sample 1.

Figure 9 presents the compression test results of conventional NiTi. The material exhibits shape memory properties with 95% martensite phase. The maximum reverse transformation strain of 3.65% is comparable to that of powder bed fusion manufactured NiTi. However, degradation is more pronounced for the conventional NiTi. After 15 compression cycles, the reverse transformation strain of conventional NiTi is measured with 2.04%, which is a percentual degradation from the first to the 15th cycle of 44%. The highest percentual degradation for powder bed fusion manufactured NiTi with shape memory properties is 21%, nearly half compared to conventional NiTi. The reason is the higher dislocation density in the parts manufactured with powder bed fusion, leading to dislocation strengthening and decreased degradation during cycling testing [33].

3.6 Hardness

The hardness behavior of NiTi manufactured with powder bed fusion is complex and influenced by several factors. Figure 10 displays the results of hardness measurements under different conditions. For as-built samples, the hardness drops from 241 HV1 to a minimum of 198 HV1 as energy density is increased from 74 to 133 J/mm^3. Subsequently, there is an increase in hardness reaching a maximum of 274 HV1 at 222 J/mm^3. Similar behavior was also observed by Nespoli et al. [14]. The hardness behavior for the as-built condition is influenced by several factors. Martensite has a lower hardness compared to austenite [34]. Lower energy densities result in lower austenite finish temperatures, increasing the proportion of austenite phase at room temperature, which leads in turn to a rise in hardness. Furthermore, the formation of finer grains when using lower energy densities

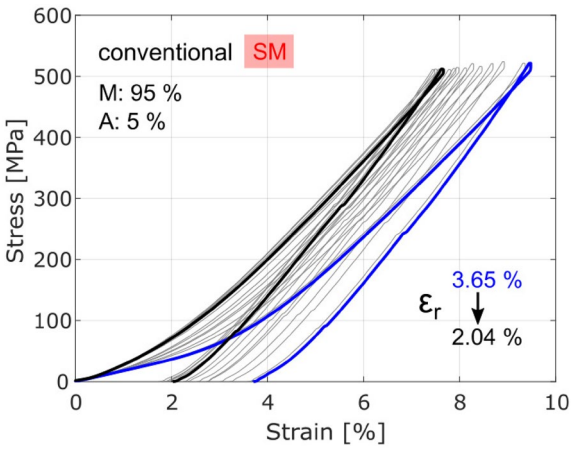

Fig. 9 Compression test of conventional NiTi with 55 wt% Ni content for cycle one (blue) and cycle 15 (black)

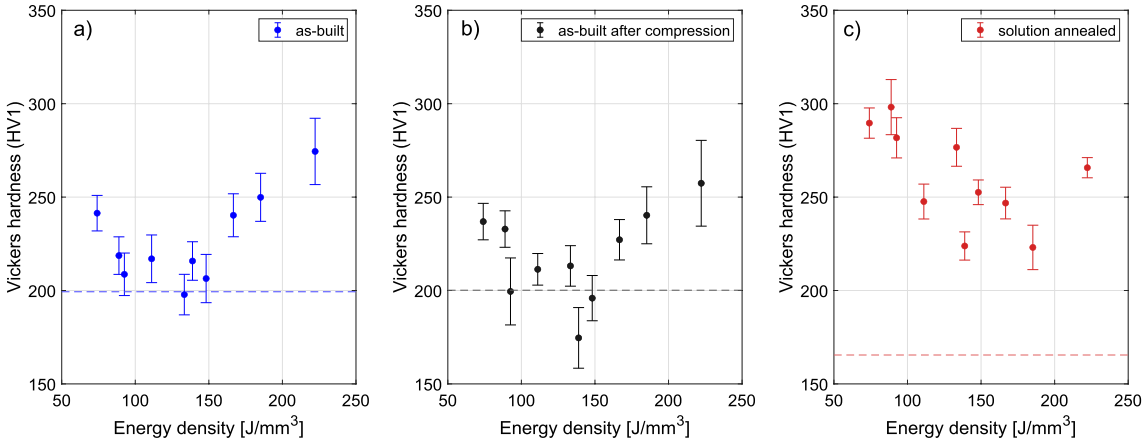

Fig. 10 Vickers hardness HV1 plotted against energy densities for **a** as-built, **b** as-built after 15 compression cycles, and **c** solution annealed condition. The dotted line represents the hardness of conventional NiTi. Only data of sample 7 are plotted from the same energy density samples of 111 J/mm^3

also contributes to a higher hardness [35]. The significant factor contributing to high hardness at lower energy densities is the higher Ni content compared to higher energy densities [36]. As energy density increases, the proportion of martensite and larger grains increases, while Ni content decreases resulting in decreasing hardness. At 133 J/mm^3, a minimum in hardness is observed, followed by an increase in hardness again with increasing energy densities. Despite the continuation of Ni depletion for increasing energy densities, there seem to be counteracting factors that lead to an overall increase in hardness after the minimum in hardness at 198 HV1 is surpassed. Ni_4Ti_3 precipitates, responsible for the double peak transformation in Fig. 4a, contribute to the increasing hardness [37]. Furthermore, the presence of impurities at higher energy densities can result in the formation of hard and brittle Ti-rich oxides, such as TiO_2, which can lead also to a steep increase in hardness.

After compression tests, the hardness of the samples is measured. No significant change in hardness is observed, indicating minimal work hardening. Even a slight tendency of decrease in hardness can be noticed. After solution annealing, precipitates are mostly solutionized and the microstructure is homogenized. There is only a slight decrease in hardness for higher energy densities (185 and 222 J/mm^3), while the hardness for medium- and low-energy densities is elevated compared to the as-built condition. A maximum hardness of 298 HV1 is measured for 89 J/mm^3, gradually decreasing to 223 HV1 for 185 J/mm^3, with the exception of the hardness for 222 J/mm^3. The hardness in the solution annealed condition is strongly influenced by the Ni content, with lower energy densities resulting in higher Ni content and hardness. The cooling rate of 1.7 °C/s could not completely prevent precipitates for energy densities 167–222 J/mm^3, as evident in the double-peak DSC curves in Fig. 4b. These precipitates counteract the influence of Ni depletion on the hardness.

3.7 Complex graded monolithic structure

To incorporate different transformation temperatures within a single part using powder bed fusion process parameters, a complex demonstrator structure in the shape of a flower is built, as shown in Fig. 11. The leaf sections of the flower were built with two different process parameters, dividing them into low and high transformation temperatures. The low transformation temperature region is achieved using a low-energy density of 93 J/mm^3, while the high transformation temperature is realized with an energy density of 167 J/mm^3, marked in blue and red, respectively, in Fig. 11c. The specific process parameters are listed in Table 1. The remaining sections of the flower are processed using an energy density of 74 J/mm^3 and were not considered for actuation.

For actuation, the marked leaves of the as-built flower shown in 11a–c are bent downwards, causing the flower to open. Subsequently, the flower was immersed in a silicon oil bath warmed up above Af temperature using a heating plate. The heating process was controlled using feedback from a thermocouple. To prevent excessive and uncontrolled heating through the contact of the flower base and the glass beaker, a rubber polymer with low thermal conductivity was placed in between. The actuation sequence is shown in Fig. 11(1–4). In sequence 1, the outer leafs with low transformation temperatures begin to fold at 25.4 °C. In sequence 2, the inner leafs with high transformation temperature begin to fold at 36.5 °C. Due to a slight overlap of the DSC curves, the inner leaves already start to fold before the transformation of the outer leaves is completed. At 47.7 °C in sequence

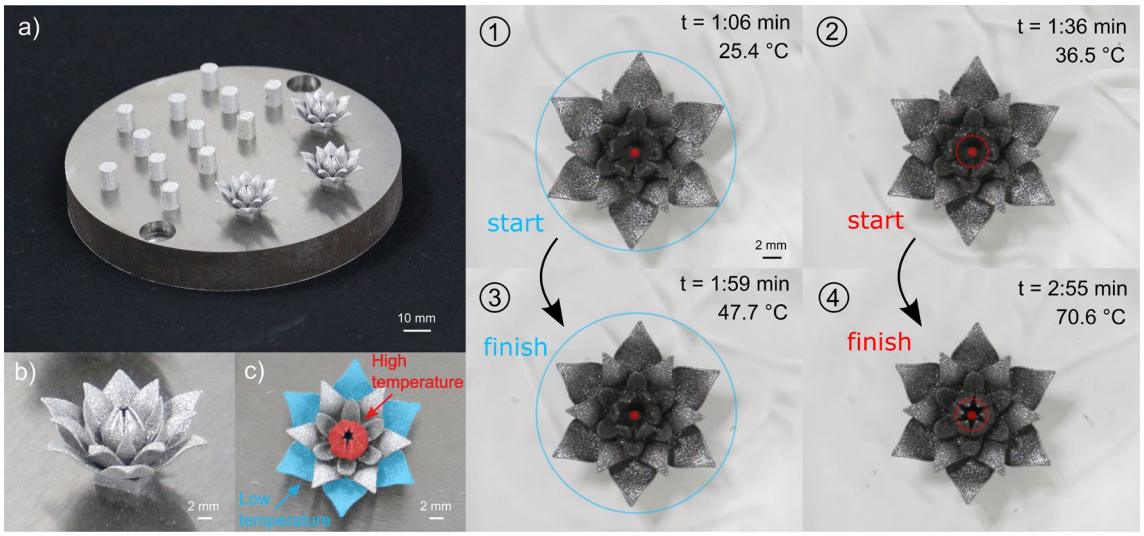

Fig. 11 Complex graded structure built with powder bed fusion. **a** Buildplate with flowers. **b** Close-up view of flower. **c** Sections of low temperature (blue) and high temperature (red) built with 93 and 167 J/mm^3, respectively. The austenite finish temperatures (Af) are 45 and 70 °C, respectively. 1) Start folding of low temperature outer leaves, 2) start folding of high temperature inner leaves, 3) finish folding of low temperature outer leaves, 4) finish folding of high temperature inner leaves. The blue and red circles are fixed references to visualize the movement of the leaves

3, the movement of the outer leaves is completed. Finally, in sequence 4 at 70.6 °C, the movement of the inner leaves is also completed. The difference between the final state shown in Fig. 11 in sequence 4 and the as-built state (c) is due to irreversible strain which cannot be recovered.

The unique capability of powder bed fusion to manufacture sections with different process parameters enables tailoring the properties of the final part. Complex structures with thermal gradients and monolithic structures can be manufactured, allowing for spatial control. The demonstrative flower illustrated the sequential actuation of monolithic parts using different austenite finish temperatures. This opens up possibilities for implementing complex displacement patterns, leading to novel applications in robotics, biomedical and aerospace industries through structural design, and adaptation of process parameters.

4 Conclusion

In this study, the processing of NiTi with powder bed fusion is investigated with a focus on the ability to vary process parameters to manufacture functionally graded structures. A maximum relative material density of 99.4% is achieved, with the flexibility to vary the energy density from 74 to 148 J/mm^3 to tune the functional properties of the manufactured samples without compromising the material density. The transformation behavior of NiTi could be adjusted by employing different process parameter combinations and energy densities. Higher energy densities result in higher transformation temperatures due to Ni evaporation. The austenite finish temperature, which is crucial for triggering actuating applications of NiTi, could be shifted between 29 ± 5 °C and 72 ± 5 °C.

Through a solution annealing process, it is possible to lower the transformation temperatures by 33 °C. The same energy densities but different process parameters result in different transformation behaviors due to the high sensitivity of chemical composition to melt pool variations. Therefore, energy densities with different parameter combinations are not comparable and should be used with caution when tuning functionally graded structures. In the cross-section variation and parameters examined in this study, no significant influence of geometry on transformation behavior is observed. However, the literature reports geometrical influences for energy densities ≤ 60 J/mm^3, which disappear for higher energy densities. There is a threshold beyond which geometrical variations need to be considered when aiming for a specific transformation behavior.

Compression tests reveal maximum reverse transformation and superelastic strains of 4.16 and 7 %, respectively, which fall within the range reported in the other studies, despite high chamber oxygen content during processing. The maximum reverse transformation strain of NiTi processed with powder bed fusion exceeds conventionally manufactured shape memory NiTi by 14%. The superelastic strain of 7% was also comparable to conventional NiTi in the literature. Hardness studies are essential for bending and actuation applications. Hardness for as-built NiTi is influenced by a variety of factors, resulting in high hardness for low- and

high-energy densities, and low hardness for medium-energy density. After solution annealing, the hardness is primarily determined by the Ni content.

Promising results are reported within this study regarding the functional performance of powder bed fusion processed NiTi, which can keep up well with the conventional NiTi. One clear advantage of powder bed fusion over conventional manufacturing is the ability to set specific transformation temperatures and functional properties in complex-shaped NiTi parts, which is successfully demonstrated. This capability could drive the development of novel applications in robotics, aerospace, and biomedical fields.

Acknowledgements The authors would like to thank Hans Rudolf Elsener (EMPA, Switzerland) for support with the heat treatment and Xiebin Wang (Shandong University, China) for the kind discussions.

Author contributions Rico Weber: conceptualization, investigation, methodology, formal analysis, visualization, validation, writing—original draft, and writing—review & editing. Enrico Tosoratti: writing—review & editing. Adriaan B. Spierings: writing—review & editing. Konrad Wegener: writing—review & editing, and supervision

Funding Open access funding provided by Swiss Federal Institute of Technology Zurich. No funding was received for conducting this study.

Data availability Data will be made available on request.

Declarations

Conflict of interest The authors declare that they have no known competing financial interests or personal relationships that could have appeared to influence the work reported in this paper.

References

1. Duerig TW (ed) (1990) Engineering aspects of shape memory alloys. Butterworth-Heinemann, London
2. Amirhesam A, Hashem Z, Shayesteh MN, Hamdy I, Samir HM, Mohammad E (2016) On the advantages of superelastic niti in ankle foot orthoses. Volume 2: Modeling, simulation and control; Bio-inspired smart materials and systems; energy harvesting. American Society of Mechanical Engineers, New York
3. Velmurugan C, Senthilkumar V, Dinesh S, Arulkirubakaran D (2018) Machining of niti-shape memory alloys-a review. Mach Sci Technol 22(3):355–401. https://doi.org/10.1080/10910344.2017.1365894
4. Hassan MR, Mehrpouya M, Dawood S (2014) Review of the machining difficulties of nickel-titanium based shape memory alloys. Appl Mech Mater 564:533–537. https://doi.org/10.4028/www.scientific.net/AMM.564.533
5. Weinert K, Petzoldt V (2004) Machining of niti based shape memory alloys. Mater Sci Eng A 378(1–2):180–184. https://doi.org/10.1016/j.msea.2003.10.344
6. Gustmann T, Gutmann F, Wenz F, Koch P, Stelzer R, Drossel W-G, Korn H (2020) Properties of a superelastic niti shape memory alloy using laser powder bed fusion and adaptive scanning strategies. Progr Addit Manuf 5(1):11–18. https://doi.org/10.1007/s40964-020-00118-6
7. Nashrudin MN, Razali MF, Mahmud AS (2020) Fabrication of step functionally graded niti by laser heating. J Alloys Compd 828:154284. https://doi.org/10.1016/j.jallcom.2020.154284
8. Sadashiva M, Yunus Sheikh M, Khan N, Kurbet R, Deve TM (2021) A review on application of shape memory alloys. Int J Recent Technol Eng 9(6):111–120. https://doi.org/10.35940/ijrte.F5438.039621
9. Frenzel J, George EP, Dlouhy A, Somsen Ch, Wagner MF-X, Eggeler G (2010) Influence of ni on martensitic phase transformations in niti shape memory alloys. Acta Mater 58(9):3444–3458. https://doi.org/10.1016/j.actamat.2010.02.019
10. Wang X, Jingya Y, Liu J, Chen L, Yang Q, Wei H, Sun J, Wang Z, Zhang Z, Zhao G, van Humbeeck J (2020) Effect of process parameters on the phase transformation behavior and tensile properties of niti shape memory alloys fabricated by selective laser melting. Addit Manuf 36:101545. https://doi.org/10.1016/j.addma.2020.101545
11. Gan J, Duan L, Li F, Che Y, Zhou Y, Wen S, Yan C (2021) Effect of laser energy density on the evolution of ni4ti3 precipitate and property of niti shape memory alloys prepared by selective laser melting. J Alloys Compd 869:159338. https://doi.org/10.1016/j.jallcom.2021.159338
12. Bormann T, Müller B, Schinhammer M, Kessler A, Thalmann P, de Wild M (2014) Microstructure of selective laser melted nickel-titanium. Mater Charact 94:189–202. https://doi.org/10.1016/j.matchar.2014.05.017
13. Dadbakhsh S, Speirs M, van Humbeeck J, Kruth J-P (2016) Laser additive manufacturing of bulk and porous shape-memory niti alloys: from processes to potential biomedical applications. MRS Bull 41(10):765–774. https://doi.org/10.1557/mrs.2016.209
14. Nespoli A, Grande AM, Bennato N, Rigamonti D, Bettini P, Villa E, Sala G, Passaretti F (2021) Towards an understanding of the functional properties of niti produced by powder bed fusion. Progr Addit Manuf 6(2):321–337. https://doi.org/10.1007/s40964-020-00155-1
15. Guo W, Feng B, Yang Y, Ren Y, Liu Y, Yang H, Yang Q, Cui L, Tong X, Hao S (2022) Effect of laser scanning speed on the microstructure, phase transformation and mechanical property of niti alloys fabricated by lpbf. Mater Design 215:110460. https://doi.org/10.1016/j.matdes.2022.110460
16. Haberland C, Elahinia M, Walker JM, Meier H, Frenzel J (2014) On the development of high quality niti shape memory and pseudoelastic parts by additive manufacturing. Smart Mater Struct 23(10):104002. https://doi.org/10.1088/0964-1726/23/10/104002
17. Safaei K, Abedi H, Nematollahi M, Kordizadeh F, Dabbaghi H, Bayati P, Javanbakht R, Jahadakbar A, Elahinia M, Poorganji B (2021) Additive manufacturing of niti shape memory alloy for biomedical applications: review of the lpbf process ecosystem. JOM 73(12):3771–3786. https://doi.org/10.1007/s11837-021-04937-y
18. Mukherjee T, Zuback JS, De A, DebRoy T (2016) Printability of alloys for additive manufacturing. Sci Reports 6:19717. https://doi.org/10.1038/srep19717
19. Zhenglei Y, Zezhou X, Guo Y, Xin R, Liu R, Jiang C, Li L, Zhang Z, Ren L (2021) Study on properties of slm-niti shape memory

alloy under the same energy density. J Mater Res Technol 13:241–250. https://doi.org/10.1016/j.jmrt.2021.04.058
20. Elahinia MH, Hashemi M, Tabesh M, Bhaduri SB (2012) Manufacturing and processing of niti implants: a review. Progr Mater Sci 57(5):911–946. https://doi.org/10.1016/j.pmatsci.2011.11.001
21. Moghaddam NS, Saedi S, Amerinatanzi A, Hinojos A, Ramazani A, Kundin J, Mills MJ, Karaca H, Elahinia M (2019) Achieving superelasticity in additively manufactured niti in compression without post-process heat treatment. Sci Reports 9(1):41. https://doi.org/10.1038/s41598-018-36641-4
22. Duerig TW, Bhattacharya K (2015) The influence of the r-phase on the superelastic behavior of niti. Shape Memory Superelast 1(2):153–161. https://doi.org/10.1007/s40830-015-0013-4
23. Gottardi G, Pola A, La Vecchia GM (2015) Solid fraction determination via dsc analysis, La Metallurgia Italiana
24. Khoo ZX, An J, Chua CK, Shen YF, Kuo CN, Liu Y (2018) Effect of heat treatment on repetitively scanned SLM NiTi shape memory alloy. Materials 12(1):77. https://doi.org/10.3390/ma12010077
25. Liu Y, Xie Z, van Humbeeck J, Delaey L, Liu Y (2000) On the deformation of the twinned domain in niti shape memory alloys. Philos Mag A 80(8):1935–1953. https://doi.org/10.1080/01418610008219095
26. Meier H, Haberland C, Frenzel J (2011) Structural and functional properties of niti shape memory alloys produced by selective laser melting. In: Bártolo P, de Lemos A, Tojeira A, Pereira A, Mateus A, Mendes A, dos Santos C, Freitas D, Bártolo H, Almeida H, dos Reis I, Dias J, Domingos M, Alves N, Pereira R, Patrício T, Ferreira T (eds) Innovative developments in virtual and physical prototyping. CRC Press, Boca Raton, pp 291–296
27. Eggeler G, Khalil-Allafi J, Gollerthan S, Somsen C, Schmahl W, Sheptyakov D (2005) On the effect of aging on martensitic transformations in ni-rich niti shape memory alloys. Smart Mater Struct 14(5):S186–S191. https://doi.org/10.1088/0964-1726/14/5/002
28. Jiang S, Zhang Y, Zhao Y, Liu S, Hu L, Zhao C (2015) Influence of ni4ti3 precipitates on phase transformation of niti shape memory alloy. Trans Nonferrous Metals Soc China 25(12):4063–4071. https://doi.org/10.1016/S1003-6326(15)64056-0
29. Bormann T, Schumacher R, Müller B, Mertmann M, de Wild M (2012) Tailoring selective laser melting process parameters for niti implants. J Mater Eng Perform 21(12):2519–2524. https://doi.org/10.1007/s11665-012-0318-9
30. Cao Y, Zhou X, Cong D, Zheng H, Cao Y, Nie Z, Chen Z, Li S, Ning X, Gao Z, Cai W, Wang Y (2020) Large tunable elastocaloric effect in additively manufactured ni-ti shape memory alloys. Acta Mater 194:178–189. https://doi.org/10.1016/j.actamat.2020.04.007
31. Saedi S, Moghaddam NS, Amerinatanzi A, Elahinia M, Karaca HE (2018) On the effects of selective laser melting process parameters on microstructure and thermomechanical response of ni-rich niti. Acta Mater 144:552–560. https://doi.org/10.1016/j.actamat.2017.10.072
32. Yoo Y-I, Kim Y-J, Shin D-K, Lee J-J (2015) Development of martensite transformation kinetics of niti shape memory alloys under compression. Int J Solids Struct 64–65:51–61. https://doi.org/10.1016/j.ijsolstr.2015.03.013
33. Lin H, Hua P, Huang K, Li Q, Sun Q (2023) Grain boundary and dislocation strengthening of nanocrystalline NiTi forstable elastocaloric cooling. Scripta Materialia 226:115227
34. Wei S, Zhang J, Zhang L, Zhang Y, Song B, Wang X, Fan J, Liu Q, Shi Y (2023) Laser powder bed fusion additive manufacturing of niti shape memory alloys: a review. Int J Extreme Manuf. https://doi.org/10.1088/2631-7990/acc7d9
35. Zhu J-N, Borisov E, Liang X, Huizenga R, Popovich A, Bliznuk V, Petrov R, Hermans M, Popovich V (2022) Controlling microstructure evolution and phase transformation behavior in additive manufacturing of nitinol shape memory alloys by tuning hatch distance. J Mater Sci 57(10):6066–6084. https://doi.org/10.1007/s10853-022-07007-z
36. Wen S, Liu Y, Zhou Y, Zhao A, Yan C, Shi Y (2021) Effect of ni content on the transformation behavior and mechanical property of niti shape memory alloys fabricated by laser powder bed fusion. Optics Laser Technol 134:106653. https://doi.org/10.1016/j.optlastec.2020.106653
37. Chad Hornbuckle B, Yu XX, Noebe RD, Martens R, Weaver ML, Thompson GB (2015) Hardening behavior and phase decomposition in very ni-rich nitinol alloys. Mater Sci Eng A 639:336–344. https://doi.org/10.1016/j.msea.2015.04.079